# Temporal change of km-scale underwater sound speed structure and GNSS-A positioning accuracy

Yusuke Yokota[1], Shun-ichi Watanabe[2], Tadashi Ishikawa[2], and Yuto Nakamura[2]

[1]Institute of Industrial Science, University of Tokyo
[2]Hydrographic and Oceanographic Department, Japan Coast Guard

November 23, 2022

**Abstract**

Underwater disturbances are the largest error source in GNSS-A seafloor geodetic observation. In particular, the gradient of sound speed structure directly affects the horizontal accuracy and needs to be examined. Previous studies have not investigated its temporal change component. In this paper, we verified the assumption that the underwater gradient structure does not change significantly during GNSS-A observation for several hours through applying a modified version of an analysis software called GARPOS to actual data of SGO-A (provided by Japan Coast Guard). Obtained results suggested that this assumption holds at many observation data, and the positioning accuracy becomes better. Some non-improved observation epochs were speculated to be accompanied by structure changes for which this assumption was not valid. It is suggested that the sound speed structure change during observation will be an important research topic in GNSS-A.

# Temporal change of km-scale underwater sound speed structure and GNSS-A positioning accuracy

**Y. Yokota[1], S. Watanabe[2], T. Ishikawa[2], and Y. Nakamura[2]**

[1]Institute of Industrial Science, University of Tokyo; Meguro-ku, Tokyo, 153-8505, Japan.

[2]Hydrographic and Oceanographic Department, Japan Coast Guard; Chiyoda-ku, Tokyo, 100-8932, Japan.

Corresponding author: Yusuke Yokota (yyokota@iis.u-tokyo.ac.jp)

**Key Points:**

- We verified the assumption that a gradient of a sound speed structure affecting GNSS-A does not change during GNSS-A observation.
- Incorporating this assumption into the analysis method improved the variation of the GNSS-A time-series.
- The results suggested the validity of the assumption and presented new research theme about the km-scale ocean structure.

**Abstract (137)**

Underwater disturbances are the largest error source in GNSS-A seafloor geodetic observation. In particular, the gradient of sound speed structure directly affects the horizontal accuracy and needs to be examined. Previous studies have not investigated its temporal change component. In this paper, we verified the assumption that the underwater gradient structure does not change significantly during GNSS-A observation for several hours through applying a modified version of an analysis software called GARPOS to actual data of SGO-A (provided by Japan Coast Guard). Obtained results suggested that this assumption holds at many observation data, and the positioning accuracy becomes better. Some non-improved observation epochs were speculated to be accompanied by structure changes for which this assumption was not valid. It is suggested that the sound speed structure change during observation will be an important research topic in GNSS-A.

**Plain Language Summary (140)**

GNSS-A is a seafloor geodetic observation method that determines the seafloor position by combining Global Navigation Satellite System (GNSS) and acoustic ranging with centimeter-scale accuracy. The biggest error in GNSS-A is not the high-rate (> 1 Hz) GNSS noise, but the kilometer-scale underwater disturbances. Previous studies have showed that the gradient of the sound speed structure strongly affects the positioning accuracy, but its time stability has not been verified. This paper has verified the assumption that the underwater structure does not change significantly during several hours in GNSS-A observation and only the intensity of the gradient may change. Incorporating this assumption into the analysis method improved the variation of the GNSS-A time-series. Thus, the kilometer-scale underwater structure was found to be generally time-stable for components that affect GNSS-A. This leads new research theme of GNSS-A seafloor geodesy and GNSS-A oceanography.

## 1 Introduction

In the last 15 years, many kinds of geophysical phenomena have been detected by a seafloor geodetic monitoring technique called as the Global Navigation Satellite System (GNSS) - Acoustic ranging combination technique (GNSS-A) proposed in 1980s (Spiess, 1985; Asada and Yabuki, 2001; Fujita et al., 2006) (fig. 1a). GNSS-A determines a seafloor position by combining high-rate (> 1 Hz) GNSS and underwater acoustic ranging on a sea surface platform such as a vessel.

Although the uncertainty of GNSS-A positioning data differs at each observation site, the standard deviation in the horizontal components (σ) is empirically about 2.0 cm and 1.5 cm in the best case in data of the GNSS-A Seafloor Geodetic Observation Array (SGO-A), provided by Japan Coast Guard (JCG) (Yokota et al., 2018). GNSS-A with this accuracy can detect temporal changes of crustal deformation by a transient postseismic effect, interplate coupling condition changes, and slow slip events (e.g., Sato et al., 2011; Yokota et al., 2016; Yokota and Ishikawa, 2020; Watanabe et al., 2021a).

Because GNSS-A is a technique which combines the radio wave positioning and acoustic wave positioning, the temporal and spatial inhomogeneity of the medium above and under the water affects the accuracy. In this paper, we focus on acoustic medium i.e., sea water. Oceanographic disturbance causing variations in under water sound speed structure (SSS) is one of the major error sources of GNSS-A. To observe the temporal change of crustal deformation, which has been actively studied in recent years (Yokota et al., 2021), the positioning accuracy of 1 cm or less is required. Therefore, high-accuracy estimation of SSS is indispensable for seismological purpose of GNSS-A and various studies have been conducted (Yokota and Ishikawa, 2019; Yokota et al., 2020; Kinugasa et al., 2020).

In the GNSS-A observation (fig. 1a) routinely operated by JCG, thousands of acoustic round-trip travel time are measured between multiple seafloor stations (acoustic transponder) and a surface station in a few hours to half a day. A surface station moves around the area where the horizontal distance is about twice the water depth and performs acoustic ranging. Here, we use the open source GNSS-A positioning software GARPOS, which enables high-precision and high-speed GNSS-A analysis (Watanabe et al., 2020; 2021b). GARPOS estimates the spatiotemporal variation of SSS in the observation area using the sufficiently many acoustic data collected from surface and seafloor stations' positions (fig. 1b).

In this paper, we examined the pattern of SSS estimated by GARPOS, using the actual data obtained at the Nankai Trough (ASZ2) and the Japan Trench (FUKU) (fig. 1c) (Japan Coast Guard, 2021), which have different ocean fields. In the Nankai Trough region (especially on its western side), the stable Kuroshio Current generates a stable SSS. On the other hand, in the Japan Trench region, SSS is more complex due to the mixing of warm water from Kuroshio and cold water from Oyashio.

## 2 SSS estimation in GARPOS

GARPOS estimates the model parameter (seafloor stations' positions and SSS as perturbations of travel time) using the residuals between observed acoustic travel time and calculated one. The round-trip travel time is calculated as a function of the seafloor stations' positions, $\boldsymbol{X}$, surface station's position, $\boldsymbol{P}(t)$, and 4-dimensional (4D) SSS, $V(e,n,u,t)$, where *e, n, u,* and *t* are eastward, northward, upward, and time components, respectively. However, since it is impossible to accurately grasp 4D-SSS, GARPOS (Watanabe et al., 2021b) estimates SSS's effect on travel time decomposing $V(e,n,u,t)$ into an effect from a horizontally stratified steady profile (reference SSS), $V_0(u)$, and a perturbation. $V_0(u)$ is obtained from sea water observation, such as Conductivity, Temperature, Depth sensors (CTD). This decomposition is expressed as following using travel time:

$$T\big(V(e,n,u,t)\big) = \exp(-\gamma)\cdot\tau\big(V_0(u)\big), \qquad (1)$$

where $\tau$ denotes the reference travel time obtained under $V_0(u)$, and $\gamma$ expresses the effect of spatiotemporal variation of SSS from the reference. Since GNSS-A has measurement points on the sea surface and seafloor only, the correction term $\gamma$ is picked up from a perturbation field expressed as a function of those positions, $\Gamma(t, \boldsymbol{P}, \boldsymbol{X})$. GARPOS version 1.0.0 implements $\Gamma$ estimation using the following linear relations as a simple function:

$$\Gamma(t, \boldsymbol{P}, \boldsymbol{X}) = \alpha_0(t) + \boldsymbol{\alpha}_1(t) \cdot \boldsymbol{P} + \boldsymbol{\alpha}_2(t) \cdot \boldsymbol{X}. \qquad (2)$$

$\alpha_0$ typically indicates the time-dependent coefficient for the average sound speed change. The coefficients for the second and third terms expresses the spatiotemporal variation of SSS depending on the surface and seafloor stations' positions.

$|\gamma| \ll 1$, where $V_0$ appropriately represents the actual SSS, is satisfied in most cases. In such cases, the deviation of actual ray path from the reference is small, so that the average sound speed along the actual path can be expressed as $\overline{V_0} + \delta V_i \sim \overline{V_0} + \gamma_i \overline{V_0}$, where $\overline{V_0}$ denotes the average of $V_0(u)$.

Fig. 2 shows the 2D schematic picture of the decomposition of SSS effect and its projection to the perturbation field, $\Gamma(t, \boldsymbol{P}, \boldsymbol{X})$. In the scheme of GARPOS, a contribution from the actual structure is lineally decomposed into ones from a steady reference profile and a residual structure. Residual structure causes a spatial variation in travel time of acoustic paths. The coefficients $\boldsymbol{\alpha}_1$ and $\boldsymbol{\alpha}_2$ in $\Gamma$ are estimated from by this spatial variation in travel time. Multiplying the $\overline{V_0}$ [m/s] by $\boldsymbol{\alpha}_1$ [km$^{-1}$] and $\boldsymbol{\alpha}_2$ [km$^{-1}$] gives characteristic gradient sound speed parameters, $\boldsymbol{g}_1(t)$ [m/s/km] and $\boldsymbol{g}_2(t)$ [m/s/km] to express the residual structure.

The representation of residual structure using $\boldsymbol{g}_1$ and $\boldsymbol{g}_2$ means that the bulk structure is projected onto functions in the boundary planes on the sea surface and seafloor. Rigidly, $\boldsymbol{P}$ and $\boldsymbol{X}$ have vertical fluctuations, but they are enough small compared to the water depth of the entire space, so they can be regarded as approximately flat surfaces. This "holographic projection" reflects the SSS as "shadow" on surface and seafloor planes.

Considering the 2D case, if a single uniform gradient layer exists at a certain depth as in fig. 2a (i.e., $\mathrm{sign}(g_1) = \mathrm{sign}(g_2)$), the characteristic depth (central depth) of the gradient layer, $D_c$, is expressed by the ratio $(\frac{g_1}{g_2})$ as the following equation (modified from eq. (32) in Watanabe et al. (2020)):

$$\frac{D_c}{D} = (1 + \frac{g_1}{g_2})^{-1}, \qquad (3)$$

where $D$ is a water depth. Because the full information of bulk SSS is partially lost by the projection to boundary, this projection is irreducible, i.e., it is not unique to inversely estimate SSS from $g_1$ and $g_2$. It is not possible to distinguish between a thick weak gradient and a thin strong gradient at almost the same depth, both of which provide the same $g_1$ and $g_2$ (Yokota, 2019). In complicated cases (fig. 2b) that cannot be assumed with a single gradient, the relationship between $g_1$ and $g_2$ becomes more complicated.

In actual case, $\boldsymbol{g}_1$ and $\boldsymbol{g}_2$ are contracted into 2D vectors with eastward and northward components, i.e., $\boldsymbol{g}_1 = (g_{1\mathrm{E}}, g_{1\mathrm{N}})$ and $\boldsymbol{g}_2 = (g_{2\mathrm{E}}, g_{2\mathrm{N}})$. To verify the 3D structure, we classify the relationship of $g_{1\mathrm{d}}$ and $g_{2\mathrm{d}}$ as $\mathbf{G}_\mathrm{d} = (g_{2\mathrm{d}}, g_{1\mathrm{d}})$ ($\mathrm{d} = \mathrm{E}, \mathrm{N}$) on the $g_{2\mathrm{d}}$–$g_{1\mathrm{d}}$ plane as shown in the right side of fig. 2. Here, we can define the angle $\theta_{\mathrm{Gd}}$ ($= \arctan(\frac{g_{1\mathrm{d}}}{g_{2\mathrm{d}}})$) as the characteristic state of SSS.

First, we consider the first and third quadrants ($\mathrm{sign}(g_{1\mathrm{d}}) = \mathrm{sign}(g_{2\mathrm{d}})$). These cases can be virtually interpreted as a single layer as fig. 2a and the characteristic depth $D_c$ of gradient layer is expressed as eq. (3). We define these quadrants as Type-I. It is possible to interpret that the structure is a single gradient layer, though it can also be a complex situation with multiple gradient layers even for the same $g_{1\mathrm{d}}$ and $g_{2\mathrm{d}}$ (Yokota, 2019). The second and fourth quadrants ($\mathrm{sign}(g_{1\mathrm{d}}) \neq \mathrm{sign}(g_{2\mathrm{d}})$) cannot be interpreted as a single layer (Type-II). In this case, SSS contains multiple characteristic scales for temporal and spatial variation. For example, it is likely to be dominated by a temporary structure such as a water intrusion (fig. 2b), which typically cannot be approximated to a linear SSS in km-scale (as fig. 2b). Therefore, the simple $\Gamma$

expression defined as eq. (2) tends to be insufficient to reflect the Type-II structures, which is a topic for future research.

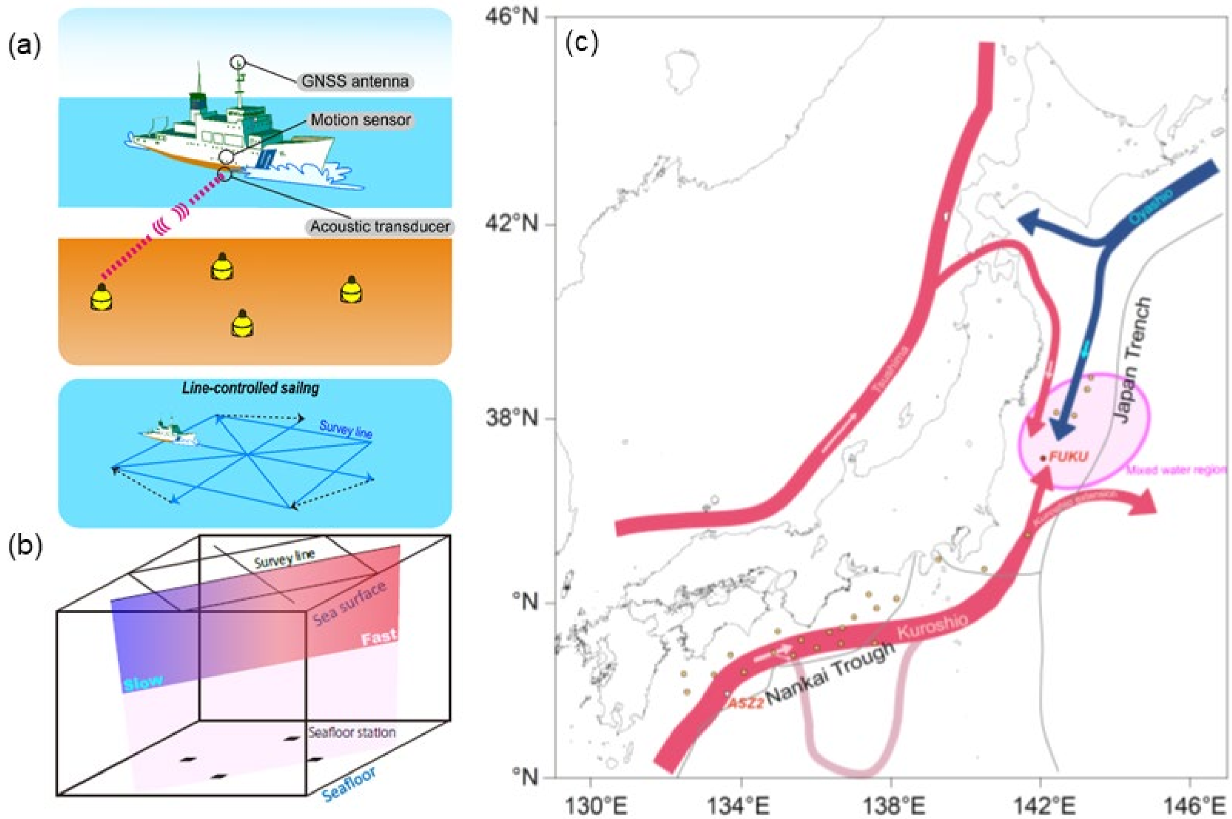


**Figure 1**. (a) A schematic of GNSS-A system (modified after Yokota et al. (2019)). (b) An example of gradient effect for the GNSS-A observation. Colored region indicates a projection of SSS on a plane. Colors indicated the sound speed. (c) The location of SGO-A sites. Currents (bold lines) and a mixed water region (purple region) are based on Yasuda et al. (1996).

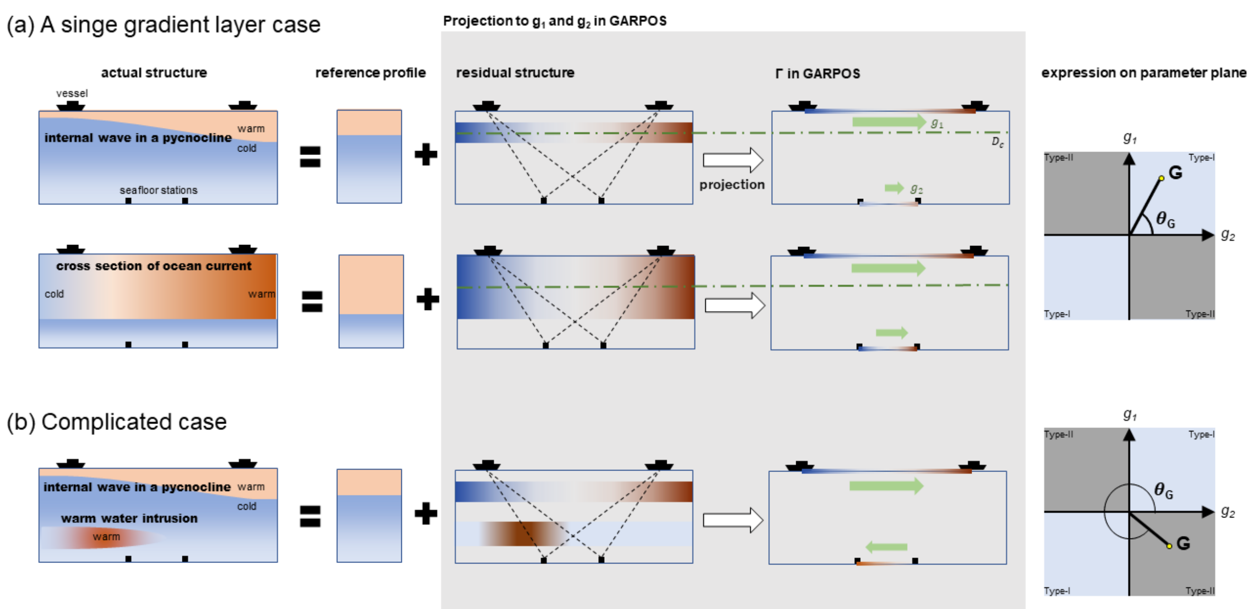


**Figure 2**. Schematic diagrams of a holographic projection in GARPOS for (a) single layer cases and (b) a complicated case. (Right) Plots of $\mathbf{G} = (g_2, g_1)$ on the 2D $g_2$–$g_1$ plane.

## 3 Constraint on G trajectory

Figs. 3a and 3b show the ASZ2 positioning time-series (northward component) estimated in GARPOS and the range of $\mathbf{G}_\mathrm{N}$ trajectories. Outliers in time-series (blue circles) are often located at boundaries across quadrants in the $\mathbf{G}_\mathrm{N}$ plane (blue-lined ellipses in fig. 3b). Figs. 3c–e show the $\mathbf{G}_\mathrm{N}$ trajectory examples of non-outlier (Jan. 2012, hereafter 2012-Jan) and outlier (2017-Jul and 2014-Sep) cases. In fig. 3c, $\mathbf{G}_\mathrm{N}$ fluctuates linearly within Type-I. On the other hand, in figs. 3d and 3e, $\mathbf{G}_\mathrm{N}$ fluctuates linearly and non-linearly, respectively, and both cross the boundary of third quadrant.

The $\mathbf{G}_\mathrm{d}$ trajectories represent the temporal variation of SSS and are interpreted as shown in fig. 4. Fig. 4a shows the simplest case, occurring the internal gravity wave in a pycnocline that is the boundary between hot and cold water, the gradient layer is generated only at a certain depth. In this case, $\mathbf{G}_\mathrm{d}$ trajectory caused by internal wave travelling is a linear trend with constant $\theta_\mathrm{Gd}$ as shown in the bottom of fig. 4a. In addition, existing a stable strong gradient field of $\theta_\mathrm{Gd} = \theta_\mathrm{Gd1}$ (e.g., due to a current) as the background, the situation becomes as shown in fig. 4b. In this case, the $\mathbf{G}_\mathrm{d}$ trajectory is a linear trend with constant $\theta_\mathrm{Gd2}$, and not passing the origin of the $\mathbf{G}_\mathrm{d}$ plane. In this simple but realistic case, the trajectory is expected to be a linear line. For more complicated case, the trajectory is no longer expected to be a linear line. For example, when the water mass intrudes into another depth, a $\mathbf{G}_\mathrm{d}$ trajectory is complicated depending on the speed of the inflow (fig. 4c) and goes through Type-II that may not express the actual SSS appropriately. 2012-Jan is close to fig. 4a or 4b and 2017-Jul and 2014-Sep are close to fig. 4c, respectively.

Here, we consider how the estimations of positions and SSS can be improved in these cases. The fluctuation of $\mathbf{G}_\mathrm{d}$ trajectory is considered to be affected by both actual SSS variation and error. In GARPOS, the bulk SSS is represented by two boundary functions $\boldsymbol{g}_1$ and $\boldsymbol{g}_2$. Therefore, $\boldsymbol{g}_1$ and $\boldsymbol{g}_2$ should be correlated to some extent. On the other hand, because $\boldsymbol{g}_2$ is strongly correlated with the seafloor station's position $\boldsymbol{X}$, the estimation of $\boldsymbol{g}_2$ is less robust than $\boldsymbol{g}_1$ due to the influence of unmodeled error sources. Therefore, the result is expected to be more reliable by adding the constraint between $\boldsymbol{g}_1$ and $\boldsymbol{g}_2$, rather than treating them as independent parameters.

Based on the relationship between the outliers and $\mathbf{G}_\mathrm{d}$ shown in fig. 3, this study introduces the assumption corresponding to fig. 4a whose gradient depth does not change over time.

Because the actual SSS variation cannot be observed directly, we evaluated the validity of this assumption from the variation of the seafloor position time-series result in next section. A correct constraint condition should reduce the time-series variation.

Here, we consider constraining $\mathbf{G}_\mathrm{d}$ on a line passing through the origin with a constant slope of $\kappa_\mathrm{d}$ as fig. 4a. This corresponds to replacing eq. (2) as follows:

$$\Gamma_2(t, \boldsymbol{P}, \boldsymbol{X}) = \alpha_0(t) + \boldsymbol{\alpha}_1(t) \cdot \boldsymbol{P} + ({\kappa_\mathrm{E}}^{-1}\alpha_{1\mathrm{E}}(t), {\kappa_\mathrm{N}}^{-1}\alpha_{1\mathrm{N}}(t), 0) \cdot \boldsymbol{X}. \quad (4)$$

Because the GARPOS version 1.0.0 dose not support the formulation of eq. (4), we performed the following two-step algorithm: In the 1st-cycle, the same analysis as GARPOS was performed using $\Gamma$ to determine $\kappa_\mathrm{d}$ using the $\mathbf{G}_\mathrm{d}$ trajectory (step-0). In the 2nd-cycle, the analysis using $\Gamma_2$ was performed constraining $\kappa_\mathrm{d}$ estimated from the 1st-cycle result.

To determine $\kappa_\mathrm{d}$ after the 1st-cycle based on the above assumption, the following flow (fig. 5a) was tried:

When $\mathbf{G}_\mathrm{d}$ is within the Type-I range and does not straddle each quadrant, $\kappa_\mathrm{d}$ was determined from the median of $\theta_{\mathrm{Gd}}$ (step-1; case-A). In other cases, to determine whether or not $\mathbf{G}_\mathrm{d}$ changes linearly, the fitting ellipse was estimated with respect to all $\mathbf{G}_\mathrm{d}$ parameters (step-2). If the semi-major axis length ($a_L$) of the estimated ellipse is more than an arbitrary ratio (*p*) with the semi-minor axis length ($a_S$), the semi-major axis direction was determined as $\kappa_\mathrm{d}$ (case-B). In this study, *p* was set to 4. For an epoch whose $\mathbf{G}_\mathrm{d}$ trajectory cannot be linearly approximated, $\kappa_\mathrm{d}$ was estimated from the median of $\theta_{\mathrm{Gd}}$ (case-C). This operation was performed individually on the eastward and northward components.

For example, 2012-Jan (fig. 3c) was classified in case-A, and $\kappa_{\mathrm{N}}$ was constrained on a dotted line and $\mathbf{G}_{\mathrm{N}}$ was determined on a blue line. 2017-Jul (fig. 3d) was classified in case-B, $\mathbf{G}_{\mathrm{N}}$, which was displaced horizontally due to an unexpected error in the 1st-cycle, was corrected. 2014-Sep (fig. 3e) was classified in case-C, $\mathbf{G}_{\mathrm{N}}$ in the Type-II range was corrected. Here, each resultant acoustic signal residual was almost unchanged and indistinguishable.

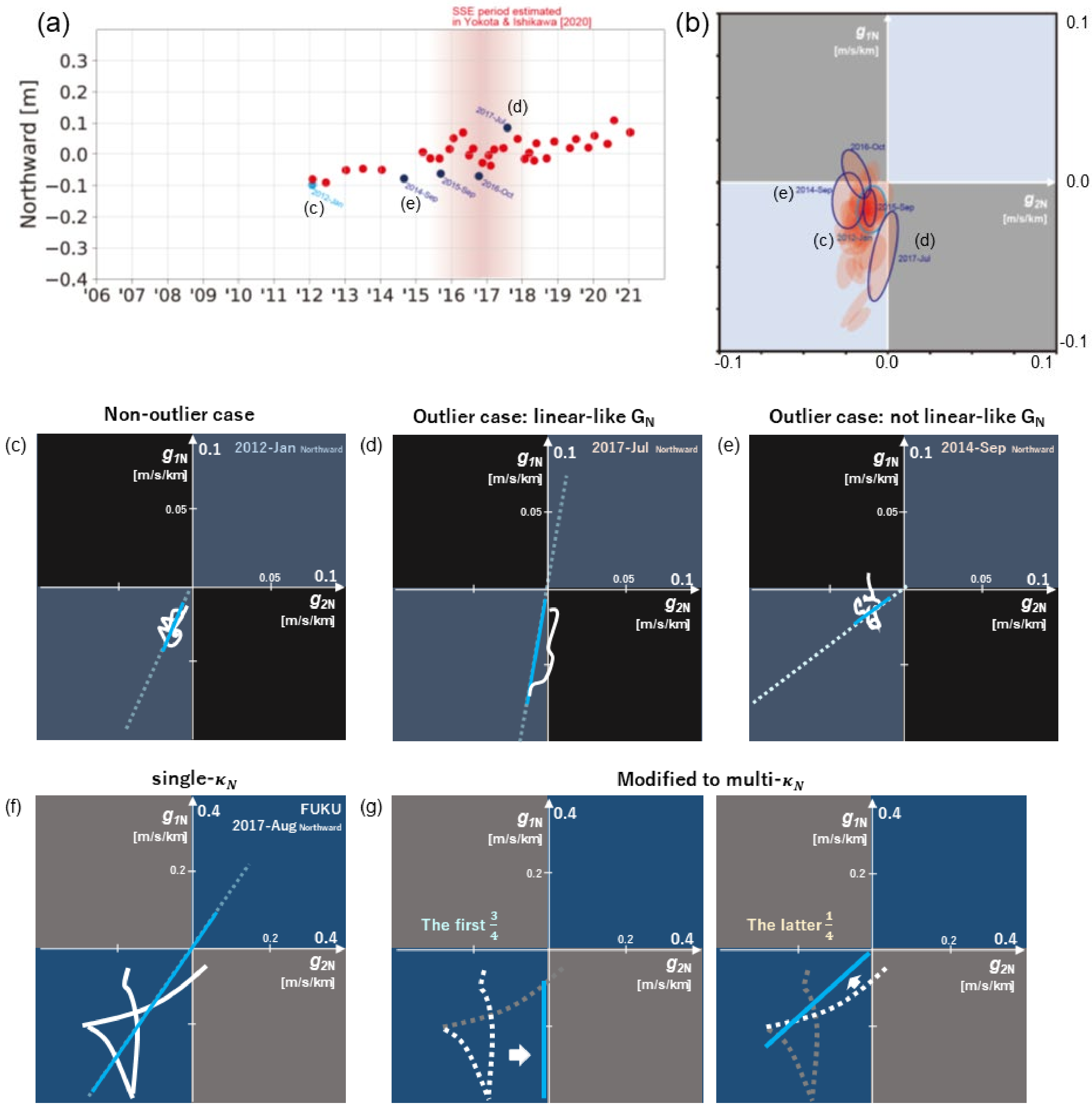


**Figure 3**. (a) The northward component of ASZ2 positioning time-series estimated in GARPOS. Pink region indicates a slow slip event period estimated in Yokota and Ishikawa (2020). Blue circles indicate outliers that deviate from the variation in surrounding epochs. Light-blue circle is

a non-outlier example. (b) Ellipses indicate the range of $\mathbf{G}_\mathrm{N}$ trajectories of all epochs. Blue-lined ellipses indicate outlier cases in (a). Light-blue-lined ellipse indicates a non-outlier example. (c–e) $\mathbf{G}_\mathrm{N}$ estimated in GARPOS (1st-cycle; white line) and the proposed 2nd-cycle (light-blue line) on the $g_{2\mathrm{N}}$–$g_{1\mathrm{N}}$ plane. Dotted line indicates the $\kappa_\mathrm{N}$ direction. (f) $\mathbf{G}_\mathrm{N}$ of 2017-Aug at FUKU. (g) $\mathbf{G}_\mathrm{N}$ estimated when the first $\frac{3}{4}$ data (left) and the latter $\frac{1}{4}$ data (right) were fixed to $\arctan(\kappa_\mathrm{N}) = \frac{\pi}{2}$ and $\frac{\pi}{4}$, respectively.

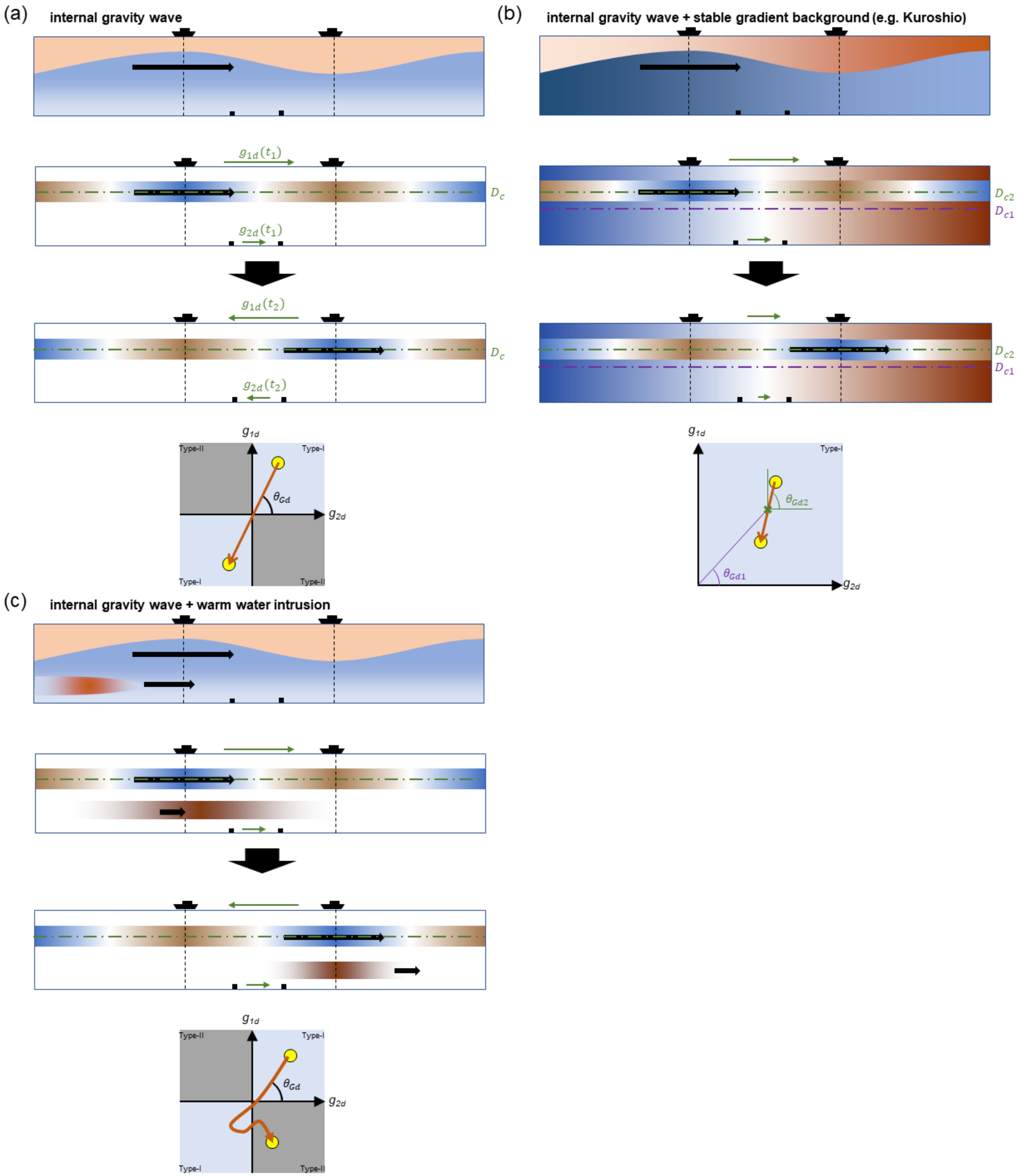


**Figure 4**. Three types of temporal changes in gradient fields from $t_1$ to $t_2$ (a) due to an internal

gravity wave, (b) in addition, due to a stable gradient background, and (c) in addition, a water intrusion. Each $\mathbf{G}_\mathrm{d}$ trajectory is drawn on the bottom.

## 4 Application of assumption

In this section, we verify the effect of constraint assumption, comparing the position time-series and estimated $\mathbf{G}_\mathrm{d}$. Figs. 5b and 5c compares the ASZ2 time-series and ranges of $\mathbf{G}_\mathrm{d}$ determined in the 1st- and 2nd-cycles.

The case-A (dark-blue circle in fig. 5b) such as the case in fig. 3c is the major pattern in the both components at ASZ2. In these cases, the variation of positioning solutions was improved by constraining the fluctuation of $\mathbf{G}_\mathrm{d}$. Outliers in the 1st-cycle time-series tend to have $\mathbf{G}_\mathrm{d}$ trajectory straddling the Type-I and Type-II regions, i.e., in case-B or C, and the positioning solutions were improved by confining $\mathbf{G}_\mathrm{d}$. This result indicates that the straddling these regions is caused by the error rather than the actual SSS variation and the constraint assumption leads a correct solution. Because ASZ2 is often located in the Kuroshio (fig. 1c), the condition that the straight $\mathbf{G}_\mathrm{d}$ does not pass through the origin strictly (fig. 4b) is expected rather than the given constraint. Therefore, there may be constraints to obtain a better time-series than the constraint given in this study (assuming fig. 4a).

For comparison, data of FUKU in the Japan Trench region (fig. 5b) was analysed with the same settings. In this site, about 80% were determined in cases-B and C, and suggesting more complicated sea conditions along the Japan Trench (fig. 1c) than ASZ2. $\kappa_\mathrm{d}$ were determined in more various directions than ASZ2 (fig. 5c), suggesting that there was no steady background SSS with strong gradient structure. FUKU results also showed the improvement in the variation of time-series, except for some outliers.

The cases where $\mathbf{G}_\mathrm{d}$ was constrained on Type-II in the 2nd-cycle (pink-lined circles) should be difficult to track SSS changes properly. However, even in those cases, there was no serious deterioration of the positioning solution. There might have been no significant $\theta_\mathrm{Gd}$ change during the observation time. The analytical handling of such cases is a further research topic.

The simple constraint assumption proposed in this study improved the accuracy of positioning solution in many cases, but some outliers still even within the Type-I remain (green-lined circles in fig. 5b). For example, in 2017-Aug at FUKU, the $\mathbf{G}_{\mathrm{N}}$ trajectory varies with time (fig. 3f). In this case, our algorithm that fixes one $\kappa_{\mathrm{N}}$ is considered not reasonable because it failed to improve the positioning solution. The positioning solution was improved (green circles in fig. 5b) when fixed with multiple $\kappa_{\mathrm{N}}$ for two divided periods (fig. 3g). The positioning solutions for some other outlier epochs were similarly improved by assuming two $\kappa_{\mathrm{d}}$ during observations (green circles in fig. 5b). In these epochs, the transition of the gradient state might have occurred in a short time. The large variation in the eastward component of the FUKU time-series suggests that such temporal change of $\theta_{\mathrm{GE}}$ might have occurred frequently.

For other outlier example, the eastward component of 2017-Dec at FUKU was classified in case-B, and the estimated positioning solution (purple-lined circle in fig. 5b) was deteriorated. This cause can be inferred from the actual observation of sound speed profiles (SSPs). Fig. S1 compares SSPs during observations of 2017-Jul at ASZ2 and 2017-Dec at FUKU. The difference of SSPs at ASZ2 is located at around 100–600 m depth. Although these observations suggest only 'SSS change over time' and do not explicitly suggest a 'gradient field,' they indicate a possibility that a gradient change at this depth. This can be regarded as a single layer shallow gradient at ASZ2 (depth: 2900 m), suggesting that the 2nd-cycle result is more appropriate than the 1st-cycle result (fig. 3d). On the other hand, the differences of SSPs at FUKU (fig. S1b) are located at around 100–400 m and 600–1000 m depths. These depths can be regarded as shallow and deep gradients at FUKU (1250 m). It suggests that validity that $\mathbf{G}_{\mathrm{N}}$ passes the Type-II range as estimated in the 1st-cycle. In this way, we can narrow down the range of $\mathbf{G}_{\mathrm{d}}$ using the SSP direct observations and a more reasonable correction of $\mathbf{G}_{\mathrm{d}}$ may be possible.

If there is only single gradient source as fig. 4a, $\frac{D_{\mathrm{cE}}}{D} = \frac{D_{\mathrm{cN}}}{D}$. If there are different gradient sources, it is possible that the effective gradient layers are different in the eastward and northward directions. When $\mathbf{G}_{\mathrm{d}}$ is decided in Type-I in the 2nd-cycle, $\frac{D_{\mathrm{cd}}}{D}$ is obtained as follow:

$$\frac{D_{\mathrm{cd}}}{D} = (1 + \kappa_{\mathrm{d}})^{-1}. \qquad (5)$$

Fig. 5d shows plots of ($\frac{D_{\mathrm{cE}}}{D}$, $\frac{D_{\mathrm{cN}}}{D}$). Many epochs at ASZ2 were determined in the range of $\frac{D_{\mathrm{cE}}}{D} \sim \frac{D_{\mathrm{cN}}}{D}$ but about half epochs at FUKU were determined to be outside those ranges. At ASZ2, $\frac{D_{\mathrm{cd}}}{D}$ were mostly located at relatively shallower side (0–0.5), suggesting a gradient field due to the Kuroshio. At FUKU, $\frac{D_{\mathrm{cd}}}{D}$ were often located at relatively deeper side, suggesting a deep gradient field close to the seafloor and the complexity of the sea condition in the Japan Trench region.

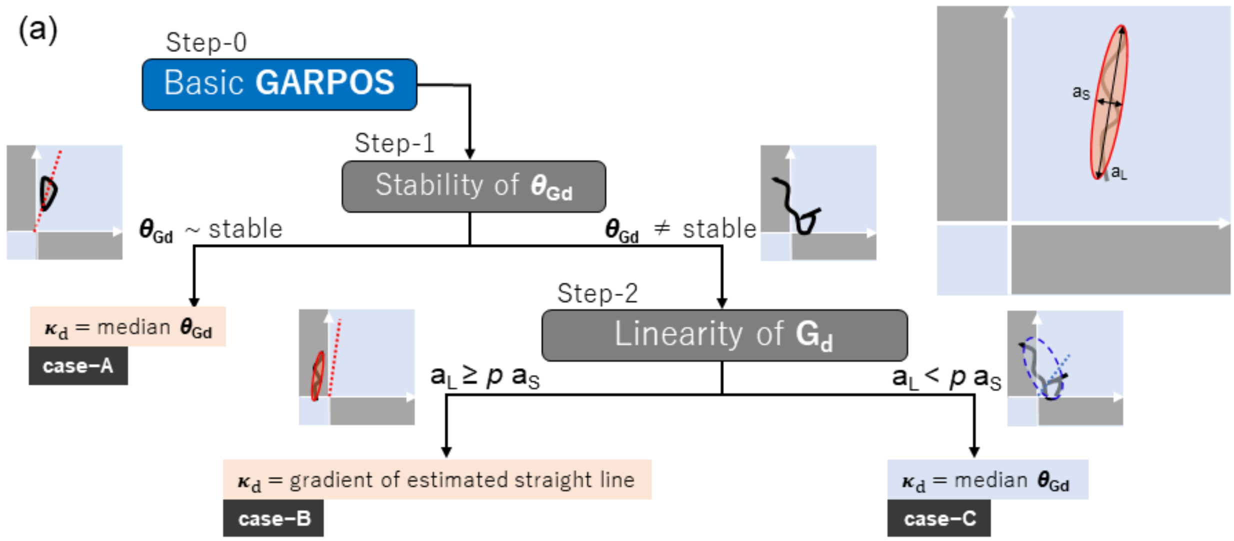
(a)
Step-0
Basic GARPOS
Step-1
Stability of $\boldsymbol{\theta}_{Gd}$
$\boldsymbol{\theta}_{Gd}$ ~ stable
$\boldsymbol{\theta}_{Gd}$ ≠ stable
$\kappa_d$ = median $\boldsymbol{\theta}_{Gd}$
case-A
Step-2
Linearity of $\mathbf{G_d}$
$a_L \geq p\, a_S$
$a_L < p\, a_S$
$\kappa_d$ = gradient of estimated straight line
case-B
$\kappa_d$ = median $\boldsymbol{\theta}_{Gd}$
case-C
$a_S$
$a_L$

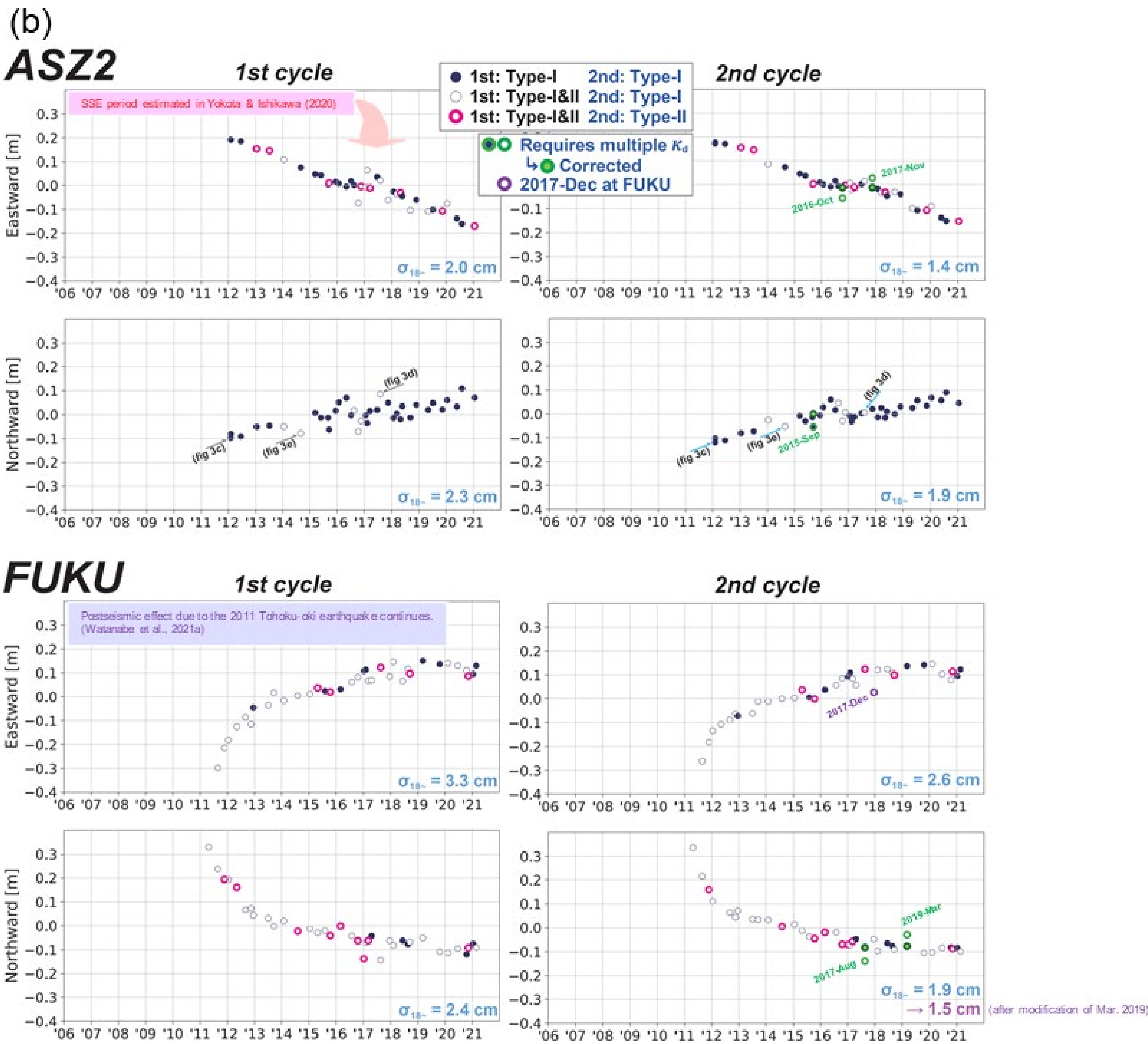

(b)
ASZ2
1st cycle
2nd cycle
SSE period estimated in Yokota & Ishikawa (2020)
1st: Type-I 2nd: Type-I
1st: Type-I&II 2nd: Type-I
1st: Type-I&II 2nd: Type-II
Requires multiple κd
Corrected
2017-Dec at FUKU
Eastward [m]
Northward [m]
σ18~ = 2.0 cm
σ18~ = 1.4 cm
σ18~ = 2.3 cm
σ18~ = 1.9 cm
2017-Nov
2016-Oct
2015-Sep
(fig 3c)
(fig 3d)
(fig 3e)
FUKU
Postseismic effect due to the 2011 Tohoku-oki earthquake continues. (Watanabe et al., 2021a)
2017-Dec
2017-Aug
2019-Mar
σ18~ = 3.3 cm
σ18~ = 2.6 cm
σ18~ = 2.4 cm
σ18~ = 1.9 cm
→ 1.5 cm
(after modification of Mar. 2019)
'06 '07 '08 '09 '10 '11 '12 '13 '14 '15 '16 '17 '18 '19 '20 '21


283

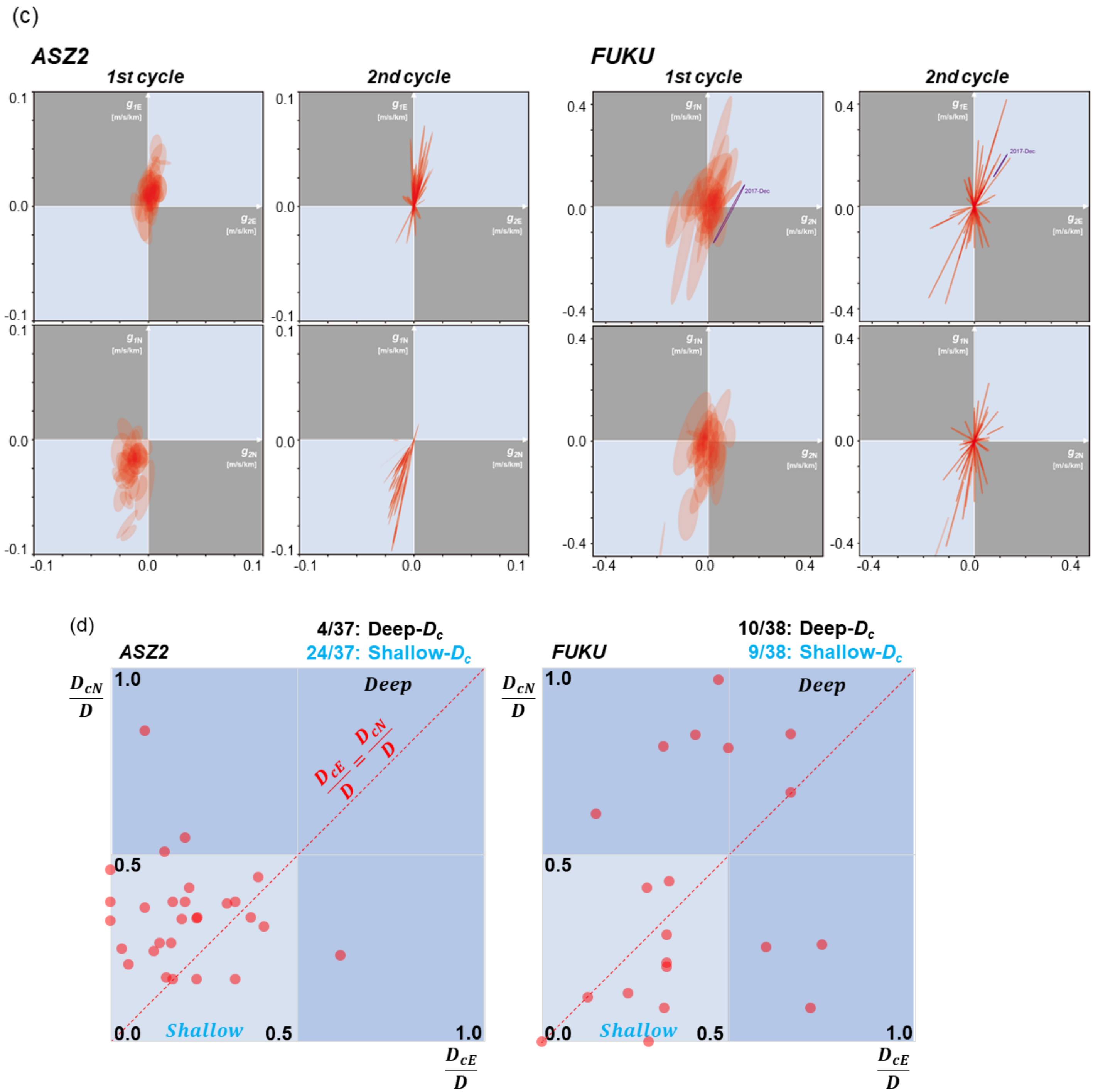


**Figure 5.** (a) Proposed algorithm flow for determining $\kappa_{\mathrm{d}}$ considering $\mathbf{G}_{\mathrm{d}}$ changes. (b) Comparison of the GARPOS ver 1.0.0 solution (1st-cycle) and the 2nd-cycle positioning solution (ASZ2 and FUKU). The meanings of the circle colors are written in the legend in the graph. The 1σ on the fitted linear trend after 2018 ($\sigma_{18\sim}$) is also written by blue characters. (c) Ranges of $\mathbf{G}_{\mathrm{d}}$

(red ellipses) determined in the 1st- and 2nd-cycles for each epoch. (FUKU) Purple ranges indicate $\mathbf{G}_\mathrm{E}$ of 2017-Dec. (d) The plots of $(\frac{D_\mathrm{cE}}{D}, \frac{D_\mathrm{cN}}{D})$ estimated in the 2nd-cycle at (a) ASZ2 and (b) FUKU. Red dotted lines indicate $\frac{D_\mathrm{cE}}{D} = \frac{D_\mathrm{cN}}{D}$. The numbers at the top are the epoch ratios of $(\frac{D_\mathrm{cE}}{D} > 0.5) \cup (\frac{D_\mathrm{cN}}{D} > 0.5)$ (indicating deep-$D_\mathrm{c}$) and $(\frac{D_\mathrm{cE}}{D} \leq 0.5) \cap (\frac{D_\mathrm{cN}}{D} \leq 0.5)$ (indicating shallow-$D_\mathrm{c}$). The denominator includes the epochs in Type-II.

## 6 Summary

As a geodetic consequence, we found that the assumption that $\theta_{\mathrm{Gd}}$ is generally temporal-stable is valid in about 90% epochs excluding some outliers at two sites, and it improves the positioning accuracy. A more appropriate time-series could be obtained by finer determination flow even for the remaining less than 10% epochs. In the future, a more appropriate $\mathbf{G}_{\mathrm{d}}$ correction might be developed using SSP direct observations and frequency of complex SSS generation as the preliminary information. Instead of a secondary solution as in this paper, a method for finding a unique solution e.g., by a modification of GARPOS, which explicitly considers the temporal-stability of $\mathbf{G}_{\mathrm{d}}$, might be also developed. The time-stability of $\mathbf{G}_{\mathrm{d}}$ is also one of the keys for understanding the tendency of narrow km-scale ocean fields in the open ocean. In particular, it is valuable in marine acoustic engineering and may contribute to its future development.

## Acknowledgments

This study was supported by ERI JURP 2021-Y-KOBO25 in Earthquake Research Institute, the University of Tokyo. Figure 1c was prepared using Generic Mapping Tools (Wessel et al., 2019).

## Data Availability Statement

The GNSS-A data and analysis software "GARPOS v1.0.0" are available at Zenodo (Japan Coast Guard, 2021; Watanabe et al., 2021b); (https://doi.org/10.5281/zenodo.5802560 and https://doi.org/10.5281/zenodo.4522027).

## References

Asada, A., and Yabuki T. (2001). Centimeter-level positioning on the seafloor. *Proc. Jpn. Acad. Ser B* 77, 7–12, https://doi.org/10.2183/pjab.77.7

Fujita, M., Ishikawa, T., Mochizuki, M., Sato, M., Toyama, S., Katayama, M., Kawai, K., Matsumoto, Y., Yabuki, T., Asada, A., and Colombo, O. L. (2006). GPS/Acoustic seafloor geodetic observation: method of data analysis and its application. *Earth Planet. Space* 58, 265–275, https://doi.org/10.1186/BF03351923

Geng, J., Jiang, P., and Liu, J. (2017). Integrating GPS with GLONASS for high-rate seismogeodesy. *Geophys. Res. Lett.*, 44, 3139–3146. https://doi.org/10.1002/2017GL072808

Japan Coast Guard (2021). GNSS-A data obtained at the sites along the Japan Trench from March 2011 to January 2021. *Zenodo*, https://doi.org/10.5281/zenodo.5802560

Kinugasa, N., Tadokoro, K., Kato, T., and Terada, Y. (2020). Estimation of temporal and spatial variation of sound speed in ocean from GNSS-A measurements for observation using moored buoy. *Prog. Earth Planet. Sci.* 7, 21. https://doi.org/10.1186/s40645-020-00331-5

Sato, M., Ishikawa, T., Ujihara, N., Yoshida, S., Fujita, M., Mochizuki, M., and Asada, A. (2011). Displacement above the hypocenter of the 2011 Tohoku-oki earthquake. *Science* 332, 1395. https://doi.org/10.1126/science.1207401

Spiess, F. (1985). Suboceanic geodetic measurements. *Geosci. Remote Sensing*, GE-23(4), 502–510, https://doi.org/10.1109/TGRS.1985.289441

Watanabe, S., Bock, Y., Chadwell, C. D., Fang, P., and Geng, J. (2017). Long-term stability of the kinematic Precise Point Positioning for the sea surface observation unit compared with the baseline analysis. *Rep. Hydro. Ocean. Res.* 54, 38–73

Watanabe, S., Ishikawa, T., Yokota, Y., and Nakamura, Y. (2020). GARPOS: Analysis software for the GNSS-A seafloor positioning with simultaneous estimation of sound speed structure. *Front. Earth Sci.* 8, 597532, https://doi.org/10.3389/feart.2020.597532

Watanabe, S., Ishikawa, T., Nakamura, Y., and Yokota, Y. (2021a). Co- and postseismic slip behaviors extracted from decadal seafloor geodesy after the 2011 Tohoku-oki earthquake. *Earth Planets Space* 73, 162. https://doi.org/10.1186/s40623-021-01487-0

Watanabe, S., Ishikawa, T., Yokota, Y., and Nakamura, Y. (2021b). GARPOS: Analysis tool for GNSS-Acoustic seafloor positioning (Version 1.0.0). *Zenodo*, https://doi.org/10.5281/zenodo.4522027

Wessel, PL., Luis, JF., Uieda, L., Scharroo, R., Wobbe, F., Smith, W. H. F., and Tian, D. (2019). The Generic Mapping Tools version 6. *Geochem. Geophys. Geosyst.* 20, 5556–5564. https://doi.org/10.1029/2019GC008515

Yasuda, I., Okuda, K., Shimizu, Y. (1996). Distribution and modification of north Pacific intermediate water in the Kuroshio–Oyashio interfrontal zone. *J. Phys. Oceanogr.*, 26, 448–465. https://doi.org/10.1175/1520-0485(1996)026<0448:DAMONP>2.0.CO;28

Yokota, Y., Ishikawa, T., Watanabe, S., Tashiro, T., and Asada A. (2016). Seafloor geodetic constraints on interplate coupling of the Nankai Trough megathrust zone. *Nature* 534, 374–377. https://doi.org/10.1038/nature17632

Yokota, Y., Ishikawa, T., and Watanabe, S. (2018). Seafloor crustal deformation data along the subduction zones around Japan obtained by GNSS-A observations. *Sci. Data* 5, 180182. https://doi.org/10.1038/sdata.2018.182

Yokota, Y. (2019). Quantitative interpretation of the ability of the GNSS-A to monitor underwater structure. *J. Marine Acoust. Soc. Jpn.* 46, 3, 116–129. https://doi.org/10.3135/jmasj.46.116

Yokota, Y., and Ishikawa, T. (2019). Gradient field of undersea sound speed structure extracted from the GNSS-A oceanography: GNSS-A as a sensor for detecting sound speed gradient. *SN Applied Sciences* 1, 693. https://doi.org/10.1007/s42452-019-0699-6

Yokota, Y., Ishikawa, T., and Watanabe, S. (2019). Gradient field of undersea sound speed structure extracted from the GNSS-A oceanography. *Mar. Geophys. Res.* 40, 493–504. https://doi.org/10.1007/s11001-018-9362-7

Yokota, Y., and Ishikawa, T. (2020). Shallow slow slip events along the Nankai Trough detected by GNSS-A. *Sci. Adv.* 6, eaay5786. https://doi.org/10.1126/sciadv.aay5786

Yokota, Y., Ishikawa, T., Watanabe, S., and Nakamura, Y. (2020). Kilometer-scale sound speed structure that affects GNSS-A observation: case study off the Kii channel. *Front. Earth Sci.* 8, 331. https://doi.org/10.3389/feart.2020.00331

Yokota, Y., Ishikawa, T., Watanabe, S., and Nakamura, Y. (2021). Crustal deformation detection capability of the GNSS-A seafloor geodetic observation array (SGO-A), provided by Japan Coast Guard. *Prog. Earth Planets Sci.* 8:63. https://doi.org/10.1186/s40645-021-00453-4

AGU PUBLICATIONS

*Geophysical Research Letters*

Supporting Information for

**Temporal change of km-scale underwater sound speed structure and GNSS-A positioning accuracy**

Y. Yokota[1], S. Watanabe[2], T. Ishikawa[2], and Y. Nakamura[2]

[1]Institute of Industrial Science, University of Tokyo; Meguro-ku, Tokyo, 153-8505, Japan.

[2]Hydrographic and Oceanographic Department, Japan Coast Guard; Chiyoda-ku, Tokyo, 100-8932, Japan.

## Contents of this file

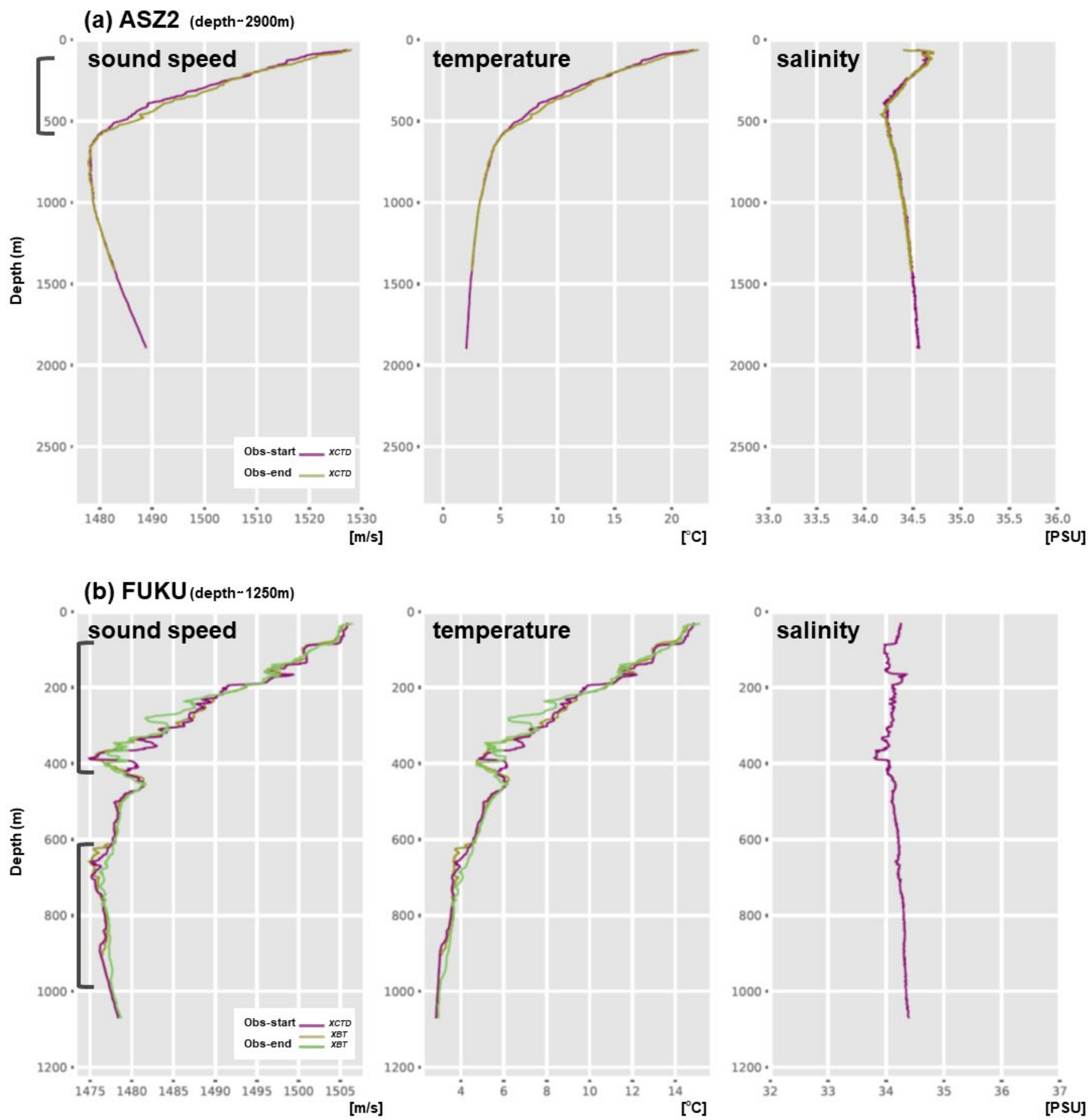


**Figure S1**. Sound speed, temperature, and salinity profile observation results on (a) 2017-Jul at ASZ2 and (b) 2017-Dec at FUKU. Differences were measured by observing multiple times (colored lines) during each observation epoch and were observed at depths of (a) 100–600 m and (b) 100–400 m and 600–1000 m, respectively (indicated by black brackets). These were monitored by expendable bathythermographs (XBT) and expendable conductivity temperature depth (XCTD) profilers. Salinity was only monitored by XCTD.